Applied Thermal Engineering 281 (2025) 128786

Contents lists available at ScienceDirect

Applied Thermal Engineering

journal homepage: www.elsevier.com/locate/ate

Research Paper

Multiphase heat transfer analysis of air expansion process in an integrated porous media-liquid piston system

Lee Haney [a], Robert Prosser [a], Alexander Lanzon [b], Yasser Mahmoudi [a,*]

[a] The University of Manchester, Department of Mechanical and Aerospace Engineering, School of Engineering, Manchester, M13 9PL, UK
[b] The University of Manchester, Department of Electrical and Electronic Engineering, School of Engineering, Manchester, M13 9PL, UK

ARTICLE INFO

Keywords:
Liquid piston gas compressor/expander
Porous media
Near-isothermal

ABSTRACT

Liquid piston gas compressors/expanders (LPGC/E) have been proposed as a key element within isothermal compressed air energy storage (CAES) systems, due to their superior heat transfer between the working gas and the liquid piston. With improved thermal management, the LPGC/E significantly lessen temperature rise during compression and delivers the required heat during expansion, thereby enhancing round-trip efficiency compared with conventional CAES, which often relies on natural gas combustion. This paper presents a computational fluid dynamics (CFD) analysis examining the highly coupled flow and thermal fields during a high-temperature expansion stroke within an LPGC/E. Further analysis of the LPGC/E integrated with porous media inserts demonstrates the impact of inserts on promoting a near-isothermal process and improving efficiency. In the baseline cases without porous inserts, simulations were conducted under two different thermal boundary conditions at the cylinder wall: Case (i), with the wall maintained at a constant ambient temperature, and Case (ii), with the wall assumed adiabatic. Results indicate that Case (ii) achieves the highest expansion efficiency of 82.4%, compared to 79.7% in Case (i), where wall cooling occurs. For the adiabatic cylinder wall, further simulations were performed with porous media inserts under two initial thermal conditions: Case (iii), where the porous inserts and air are in thermal non-equilibrium, and Case (iv), where the two regions are in thermal equilibrium. The findings show that Case (iii) yields an expansion efficiency of 76.1%, whereas Case (iv) significantly enhances efficiency to 88.1%, outperforming the corresponding baseline (no porous inserts) case. Expansion performance is improved in Cases (ii) and (iv) by reducing heat transfer within the system, underpinning the importance of mitigating the temperature reduction and striving to achieve a near-isothermal process. These findings provide a foundation for developing more efficient LPGC/E-based isothermal CAES systems, offering guidance on optimising thermal management techniques along with porous media integration for practical energy storage applications.

1. Introduction

The increasing reliance on renewable energy sources highlights the need for efficient and scalable energy storage technologies [1]. To ensure grid stability and reliability, one novel storage method that has undergone significant development over the last decade is compressed air energy storage (CAES) [2]. As a form of long-duration energy storage, CAES provides storage ranging from days to weeks in addition to a medium-duration discharge, ranging over 4 h. Systems are classified into four main variants based on their overall thermal management: Diabatic (D-CAES), Adiabatic (A-CAES), Isothermal (I-CAES), and Near-isothermal-Adiabatic (Ni-A-CAES).

D-CAES is the most established variant, but due to its inefficient thermal management, it suffers from low (≈ 50%) round-trip efficiency (RTE) [3]. The heat generated during compression is not retained but is instead dissipated to the environment; therefore, prior to expansion, the cooled, compressed air must be reheated using external fuel combustion to enhance energy recovery. This approach diminishes the environmental advantages of the system by requiring continuous fossil fuel input and emitting greenhouse gases [4]. Nevertheless, the only commercial CAES plants in operation (Huntorf, Germany and McIntosh, USA) follow the diabatic approach due to its lower initial capital cost and technological maturity [5,6].

A-CAES strives to overcome D-CAES inefficiencies by coupling thermal energy storage (TES) to capture heat generated during compression and reintroducing it prior to expansion [7]. Storing the generated heat eliminates the need for fossil fuel combustion, enabling a carbon-free operation leading to a potential RTE increase above 70% [8].

* Corresponding author.
E-mail address: yasser.mahmoudilarimi@manchester.ac.uk (Y. Mahmoudi).

https://doi.org/10.1016/j.applthermaleng.2025.128786
Received 17 June 2025; Received in revised form 24 August 2025; Accepted 17 October 2025
Available online 20 October 2025

Nomenclature

Symbols

$\langle\rangle$	Time-averaged value (–)
c	Specific heat (J/kg · K)
g	Gravity (m/s^2)
h	Porous media length (m)
k	Turbulent kinetic energy (m^2/s^2)
L	Cylinder length (m)
P	Pressure (bar)
T	Temperature (K)
t	Time (s)
u	Fluid velocity (m/s)
V	Volume (m^3)
W	Width (m)
W	Work (J)
Co	Courant number (–)
Gr	Grashof number (–)
Pr	Prandtl number (–)
Ra	Rayleigh number (–)
Re	Reynolds number (–)
Ri	Richardson number (–)

Greek Symbols

α	Volume phase fraction (–)
$\bar{\bar{\tau}}$	Stress tensor (N/m^2)
β	Thermal expansion coefficient (–)
Δ	Difference (–)
η	Expansion efficiency (%) (–)
κ	Thermal conductivity (W/m · K)
μ	Dynamic viscosity (kg/ms)
∇	Nabla (–)
ρ	Density (kg/m^3)

Superscripts

$\bar{\phi}$	Mean

Subscripts

0	Initial
a	Air
ave	Average
c	Compressed
e	Expanded
f	Fluid
out	Output
p	Pore
p	Pressure
pm	Porous media
s	Solid
s	Stored
t	Turbulent
w	Water
$wall$	Wall
x	X-coordinate

Acronyms

3-D	Three-dimensional
A-CAES	Adiabatic compressed air energy storage
CAES	Compressed air energy storage
CFD	Computational fluid dynamics
CHT	Conjugate heat transfer
D-CAES	Diabatic compressed air energy storage
DNS	Direct numerical simulations
HTC	Heat transfer coefficient
LES	Large eddy simulations
LPGC/E	Liquid piston gas compressor/expander
Ni-A-CAES	Near-isothermal-Adiabatic compressed air energy storage
RTE	Round-trip efficiency
SA/V	Surface-area-to-volume
TES	Thermal energy storage
uRANS	Unsteady Reynolds-averaged Navier–Stokes
VOF	Volume of fluid

A-CAES requires high-temperature TES systems that can retain heat for extended periods without significant losses, posing engineering and cost challenges [9]. While several pilot projects and feasibility studies are ongoing, no large-scale commercial A-CAES system has yet been deployed [10].

I-CAES represents a technically challenging technique, which maintains the air at a nearly constant temperature throughout compression and expansion [11]. By minimising temperature fluctuations, I-CAES significantly diminishes the energy losses associated with heat dissipation and mechanical work. Theoretically, isothermal processes achieve RTEs approaching 100% [12]. However, executing true isothermal conditions at scale is technically demanding, requiring very slow compression/expansion rates or advanced heat exchange systems capable of instantaneously removing or supplying heat. Accordingly, recent research has focused on near-isothermal CAES systems [13,14].

Ni-A-CAES offers a coupled system by creating near-isothermal compression and expansion processes while employing the A-CAES design methodology of capturing, storing, and reusing the heat generated during compression [15]. Ni-A-CAES reduces the technical demand of delivering an isothermal process by allowing for some temperature variations, mitigated through the use of a heat exchanger [16]. The integration of heat exchangers enables shorter compression and expansion times to achieve a near-isothermal process and results in a significant reduction in the temperature rise compared to a case without heat exchangers [17]. Similar to A-CAES, this method eliminates the need for fossil fuel combustion, thereby improving the sustainability issues associated with D-CAES [3,4]. Managing temperatures post-compression enables the implementation of a lower-temperature TES unit, which alleviates the burden on engineering and addresses the cost issues associated with A-CAES [18].

A liquid piston gas compressor/expander (LPGC/E) simplifies system complexity by integrating the compression and expansion processes into a single unit (Fig. 1), thereby reducing the overall system design and component count [19]. The device's primary asset is its capacity to include porous media inserts that help manage heat flux during compression and expansion processes. Inserts assist in reducing the temperature rise during a compression stroke by swiftly distributing the heat [20], helping to achieve a near-isothermal process. One of the effects of mitigating the temperature increase is a substantial improvement in compression efficiency [21]. By contrast, to achieve a near-isothermal expansion process, the air temperature must be maintained at a sufficiently elevated level at the beginning of the expansion stroke.

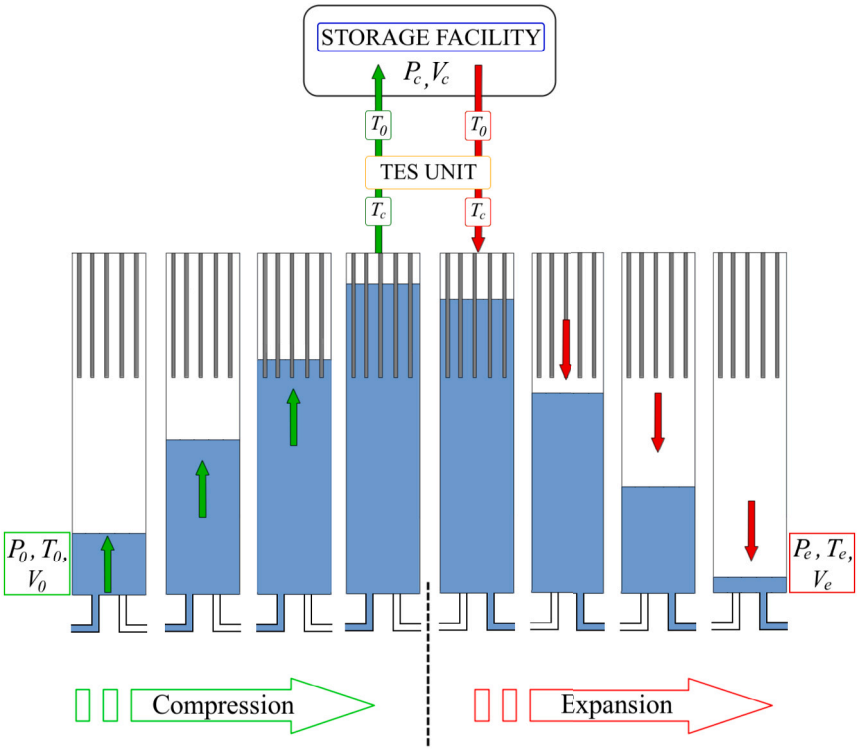

Fig. 1. Illustration of a LPGC/E fitted with porous media during both compression and expansion processes.

Several studies have been conducted applying different heat exchanger methods during compression such as cooling tubes [22], high-pressure sprays [23], aqueous foams [24] and phase change materials (PCM) [25], all of which achieve high compression process efficiencies; yet, none of the these compression improvement methods have been tested during an expansion stroke. Latent heat transfer methods, such as metal inserts, have been applied to an expansion stroke to facilitate a near-isothermal process within an LPGC/E [20,26]. Teams from the University of Minnesota apply metallic porous inserts in the form of interrupted plates and metal foams in low [26] and high pressure systems [20]. Yan et al. [26] yield efficiency improvements of 12% up to 94% when applying inserts into the low-pressure expansion cases compared to the baseline (no insert) cases. The significant increase is due to the energy transfer between the inserts and the cooling air. The expansion process initially establishes thermal equilibrium between the air and the porous inserts; however, as the process continues, the air temperature decreases significantly. In contrast, the thermal properties of the solid insert result in only a negligible temperature reduction, leading to a substantial temperature gradient forming between the air and the solid structure, promoting an energy transfer. A recovery in temperature is attained, resulting in a near-isothermal process. Wieberdink et al. [20] observed a similar non-monotonic temperature profile during their high-pressure experiments when reducing the outflow rate. Slowing the flow rate prolongs the expansion time, allowing more time for heat transfer. Gouda et al. [27] observed the same phenomena when the heat transfer occurs between the working gas and the cylinder wall, producing an anisotropic flow profile. Both studies, when the structural and fluid elements are in thermal equilibrium and a prolonged expansion takes place, result in significant efficiency improvements of approximately 96% [20] and 98% [27], respectively.

However, one aspect of the previous experimental/numerical parameters requires reconsideration, specifically the critical issue of the initial air temperature before expansion begins. In the previous studies, compressed air was stored and allowed to cool naturally, resulting in low initial temperatures (285–300 K) before expansion. A temperature reduction lowers the air pressure and non-flow exergy, limiting its capacity to perform useful work unless reheated or recompressed. To counteract the temperature drop, the flow rate at which the liquid piston is expelled from the LPGC/E can be reduced to deliver a prolonged expansion stroke and a potential near-isothermal process. This protracted method has been implemented to mitigate temperature reduction by increasing the expansion time in the previously discussed studies [20,26,27]. However, when initiating the expansion process with an elevated air temperature, the initial thermal energy is enhanced, thereby increasing the exergy within the system. One method to improve the capacity of mechanical work is to apply a heat source to help produce a near-isothermal process [23].

Another proposed method to avoid air reheating is to store the heat produced during a compression stroke via a TES unit [28]. In A-CAES or Ni-A-CAES systems, the high-temperature air will pass through a TES before entering storage [9,29]. Storing the thermal energy allows it to be retrieved before expansion, eliminating the requirement to reheat the air by burning off natural gas, as per current D-CAES technology [5,6]. Depending on the compression performance, air temperatures can reach between 340 K [27] and 650 K [20]; therefore, current expansion studies do not consider using recovered heat. When heat is not recovered, and initial ambient temperatures are used pre-expansion, the primary concern is the extremely low temperatures encountered during the expansion process [20,26,27].

Using such pre-expansion conditions can lead to extreme temperature reductions and potential unwanted frosting [30]; furthermore, operating the component at these temperatures could adversely affect its functionality [3,4]. Temperatures ranging from 141 K [20] to 222 K [26] were recorded during previous cases with no porous inserts when starting the expansion process from ambient (285–300 K), with mitigation efforts focused on increasing the expansion time. Nevertheless, temperatures still reached between 259 K [20] and 269 K [27] for a protracted expansion process.

Currently, there is limited research focused on the flow physics of the expansion process, as most LPGC/E studies concentrate on gas compression due to its broader applicability across multiple sectors, such as hydrogen [31], CO_2 [32,33] and natural gas systems [34].

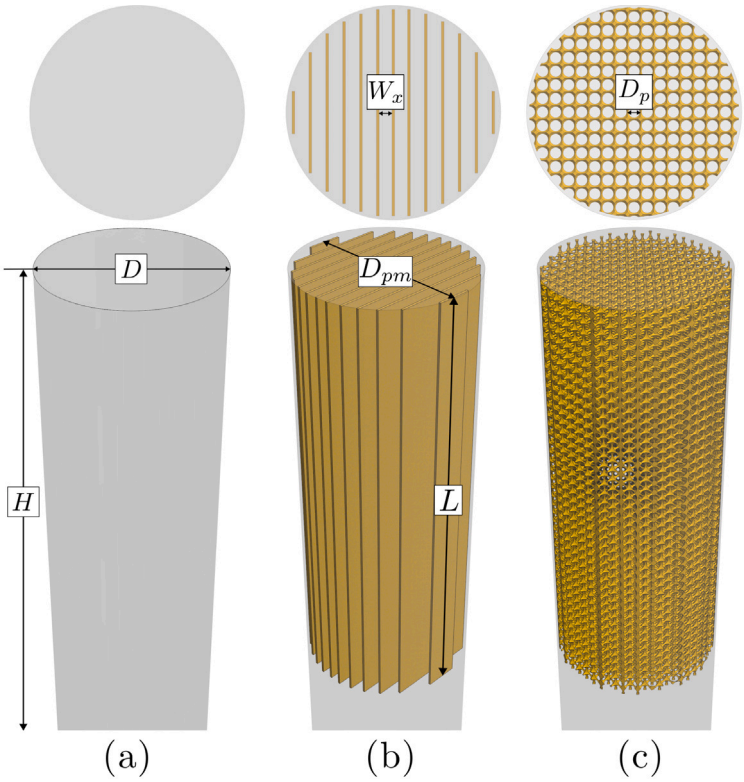

Fig. 2. 3-D LPGC/E arrangements used during numerical simulations: (a) baseline (no porous inserts), (b) parallel plates and (c) metal foam configurations.

Table 1
Thermophysical properties of LPGC/E associated parts.

Part	ρ (kg/m^3)	κ (W/m K)	c_p (J/kg K)	μ (kg/m s)
Air	Ideal gas	0.03	1006	Sutherland [35]
Water	998	0.6	4187	8.9×10^{-4}
Porous media (Aluminium)	2719	237	871	–

Therefore, the present study aims to address gaps in the literature on the expansion process by being the first to investigate a high-temperature expansion within a porous-media-integrated liquid-piston device. The study provides the following contributions:

- Analysis of the fundamental fluid dynamics and heat transfer characteristics of the expansion process, focusing on the multiphase flow interactions under elevated initial expansion air temperatures and the influence of the porous media inserts.
- Using higher initial temperatures – representative of post-compression conditions with heat recovery from a TES unit – offers a more realistic approximation of operational scenarios observed in a Ni-A-CAES configuration.
- By investigating how elevated thermal states influence flow behaviour, temperature gradients, phase interactions, and energy recovery, this study provides critical insights into achieving near-isothermal expansion and enhancing system efficiency.

2. Methodology

This investigation employs computational fluid dynamics (CFD) simulations to examine the coupled fluid mechanics and heat transfer processes during the gas expansion phase in an LPGC/E cylinder. Two cases were analysed: a baseline case (a cylinder without porous inserts) and a modified case with porous materials inserted inside the LPGC/E cylinder. The LPGC/E domain is a cylinder with a zero-thickness wall; it has a diameter (D) of 0.079 m and a length (L) of 1 m, resulting in a volume of 4.9 litres. In the LPGC/E system, air serves as the working gas and water as a liquid piston. Water fills approximately 70% of the cylinder volume prior to expansion, which represents the water volume post-compression stroke [17]. Porous inserts are introduced into the LPGC/E to assess their performance compared to the baseline case, including aluminium parallel plates with a spacing (W_x) of 5 mm per plate in the transverse direction (Fig. 2b) and a 'foam-like' lattice structure with a pore size (D_p) of 5 mm in diameter (Fig. 2c). Both inserts have a diameter (D_{pm}) of 0.077 m, allowing for a 1 mm clearance between the insert and the cylinder wall, and fixed lengths (h) of 0.2 m are used. The inserts are placed at the top of the cylinder and interact only with the air during the expansion process. Thermophysical properties for LPGC/E and the associated parts can be found in Table 1.

2.1. Governing equations

The modelling analysis considers a transient, turbulent, multiphase system comprising water, air and metallic porous inserts. An unsteady Reynolds-Averaged Navier–Stokes (uRANS) model was used to model the turbulent field, incorporating conjugate heat transfer (CHT) between the metallic porous inserts and the surrounding air [36]. An Eulerian volume-of-fluid (VOF) method was used to capture the interface between air and water by tracking the volume fraction of both

fluids and solving a single set of equations. VOF can then determine the interface location between the two fluids.

2.1.1. Multiphase Navier–Stokes

As this case uses an ideal gas, the compressible Navier–Stokes equations are applied, with the continuity equation given as [37]:

$$\frac{\partial \rho}{\partial t} + \nabla \cdot (\rho u) = 0, \tag{1}$$

with density modelled as a function of pressure and temperature:

$$\rho = \frac{p}{RT}, \tag{2}$$

and R is the ideal gas constant. The momentum equation is solved for both phases using phase-averaging [38]:

$$\frac{\partial \rho u}{\partial t} + \nabla \cdot (\rho u u) = -\nabla p + \nabla \cdot \bar{\bar{\tau}} + \rho g, \tag{3}$$

with density being a sum of both phases using

$$\rho = \alpha_a \rho_a + \alpha_w \rho_w. \tag{4}$$

The stress tensor is based on the viscosity of the air–water mixture [39],

$$\bar{\bar{\tau}} = 2\mu S - \frac{2}{3}\mu (\nabla \cdot u), \tag{5}$$

where,

$$\mu = \alpha_a \mu_a + \alpha_w \mu_w, \tag{6}$$

and S is the modulus of the mean strain rate tensor [40]:

$$S = \sqrt{2 S_{ij} S ij}. \tag{7}$$

The energy equation for the fluid mixture is modelled using the mean-phase average properties [41]:

$$\frac{\partial (\rho c_p T)}{\partial t} + \nabla \cdot (u \rho c_p T) = \nabla \cdot (\kappa_f \nabla T) + h_v (T_f - T_s), \tag{8}$$

with,

$$\kappa_f = \alpha_a \kappa_a + \alpha_w \kappa_w, \tag{9}$$

$$\rho c_p = \alpha_a \rho_a c_{p,a} + \alpha_w \rho_w c_{p,w}. \tag{10}$$

The energy equation for the solid phase (porous media) is given as [41]:

$$\frac{\partial}{\partial t}(\rho c_s T) = \nabla \cdot (\kappa_s \nabla T) + h_v (T_s - T_f). \tag{11}$$

2.2. Boundary conditions

Different flow rates are used to examine the influence of expansion rates; initially, cases use a constant mass outflow of 0.875 kg/s, equivalent to 52.5 l/min. Further cases are completed with a decreased flow rate of 0.08 kg/s, equivalent to 5 l/min; these flow rates are categorised as fast and slow expansion rates, respectively. An initial pressure of 10 bar and a temperature of 440 K are applied for all cases; these are the final conditions of our baseline compression work [17]. An adiabatic, no-slip wall boundary condition is applied to the cylinder walls in all cases except one, where a constant temperature wall boundary condition is used in a baseline case (Case (i)) consistent with the literature [27]. Using a constant wall temperature at 298 K ($T_{wall} < T_{air}$) provides a cooling feature and simulates the performance of an uninsulated LPGC/E compared to the adiabatic wall condition used in Case (ii); this temperature is selected to align with the ambient temperature used during our compression work [17]. A significant difference from the literature is the large initial ΔT between the wall and the air. In contrast, the literature typically starts in thermal equilibrium with an initial ambient temperature; this is described in further detail in Section 3.1.1.

A constant temperature boundary condition is applied to the porous media cases to investigate their impact on the expansion process, with two temperatures being imposed: Case (iii) 298 K and Case (iv) 440 K, which is in thermal equilibrium with the air. These temperatures are selected to evaluate performance at different stages of the expansion process, with Case (iii) designed to simulate the expansion process during the initial expansion strokes when the ambient plates have not been exposed to high-temperature air, thereby creating a temperature imbalance between the air and the inserts. As the expansion process undergoes multiple strokes, the inserts will be exposed to high-temperature air for an extended period, increasing their temperature; Case (iv) represents the higher-temperature (440 K) porous insert case. Furthermore, a wall constant CHT setting is applied via the solver to enable heat transfer between the inserts and the fluid [36]. Since pressures are low and temperature differences are relatively small, the air is treated as an ideal gas, with dynamic viscosity changes modelled through Sutherland's law [35].

2.3. Process efficiency

The measure of performance used throughout this study is the expansion process efficiency (η_e), which is the ratio of output work (W_{out}) to energy stored (E_s) [26]:

$$\eta_e = \frac{W_{out}}{E_s}. \tag{12}$$

When expanding gases, higher efficiency is achieved by reducing heat transfer in the system and achieving a near-isothermal process [27]. When accounting for W_{out}, we assume an isothermal process; therefore, the output work can be expressed as [26]:

$$W_{out} = (P_c - P_e)V_c + \int_{V_c}^{V_e} (P - P_e) dV. \tag{13}$$

Eq. (13) can be separated into two terms; starting with the second term, which represents the thermodynamic pressure-volume work ($\int PdV$) throughout the expansion process. The pressure and volume for the air's compressed state are given as P_c, V_c, with P_e, V_e being the respective pressure and volume values for the air's expanded state. The deviation from the standard thermodynamic work formula lies in the first term ($(P_c - P_e)V_c$) which represents an isochoric injection of compressed air into the cylinder before the work is performed [26]. When expanded from its initial conditions, E_s represents the storage energy, assessed as the work extracted from the compressed air. If the expansion is sufficiently slow, an isothermal process occurs; adiabatic conditions are encountered for fast processes. This method considers the maximum potential energy of the stored cool air when considering an isothermal expansion. Using the compressed conditions and P_c/P_e as the expansion ratio, E_s is expressed as [19]:

$$E_s = P_c V_c \ln \left| \frac{P_c}{P_e} \right|. \tag{14}$$

2.4. Simulation parameters

Within Star-CCM+, the $k-\omega$ SST model [42] is applied for closure of the turbulence equations, using segregated solvers for the flow and energy. For the transient formulation and the spatial derivatives, first-order implicit methods and a second-order upwind scheme are applied, respectively. The least squares method is used to compute the gradients of variables. For the pressure–velocity coupling, the SIMPLEC (Semi-Implicit Method for Pressure Linked Equations-Consistent) algorithm is employed. Due to the transient nature of the case, a prerequisite is having a Courant number (Co) less than 1; this condition determines a time step between 1×10^{-3} and 1×10^{-4} seconds. Larger time steps are used on the longer duration expansion cases while still satisfying the $Co < 1$ condition.

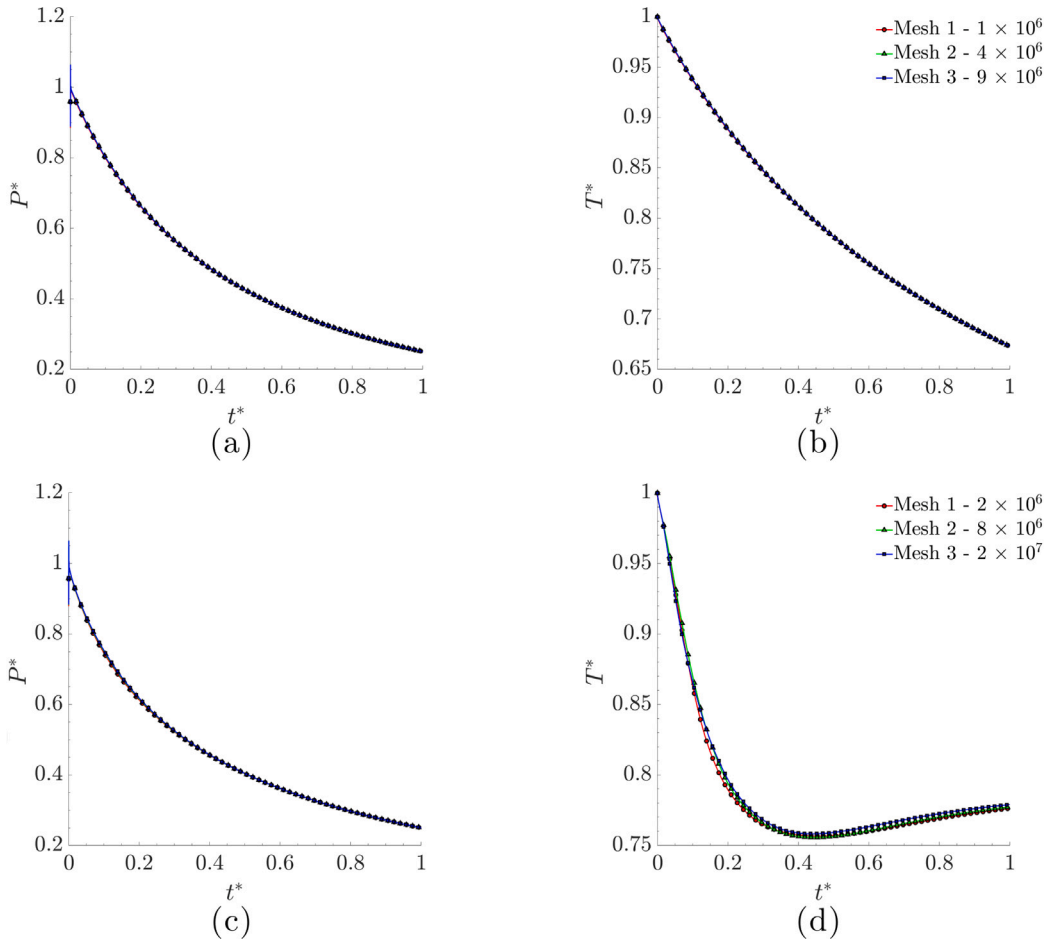

Fig. 3. Mesh independence tests for the time-dependent behaviour of normalised pressure (P^*) and temperature (T^*) in the: (1) adiabatic wall baseline case (Figures (a) and (b)) and: (2) the high-temperature parallel plate case (Figures (c) and (d)). Three successively finer meshes are examined.

2.5. Meshing

Polyhedral meshes are used for all cases, with a $y^+ < 5$ imposed throughout the entire domain, resulting in an element count ranging between 1×10^6 and 1×10^7. An increase in the element count results from the inclusion of porous media inserts and their geometric complexity. A mesh independence analysis is conducted on all cases to ensure the results are independent of the mesh resolution; however, for repeatability, only one baseline case (Figs. 3a and b) and one porous media case (Figs. 3c and d) are shown. Three meshes are tested for each case, with normalised pressure ($P^* = P/P_0$) and temperature ($T^* = T/T_0$) plotted over the normalised expansion duration ($t^* = t/t_e$), upon which the differences in P^* and T^* are $O(10^{-3})$ and $O(10^{-4})$, respectively. Therefore, mesh two was chosen for the subsequent baseline and porous media cases.

2.6. Validation

The numerical model is validated by comparison against Gouda et al.'s experimental and numerical works [27]. The results in Fig. 4 are based on an empty (no porous inserts) LPGC/E configuration, and as per the mesh independence, P^* and T^* are plotted over t^*. Discrepancies between our uRANS and Gouda's LES are $O(10^{-2})$ for P^* and T^*, with the differences being $O(10^{-3})$ compared to the experimental test data. Table 2 presents an error analysis between the current study and reference data [27]. Four locations are selected from the P^* and T^* plots, and the relative error (%) is provided for each data point. Data points locations were determined from the minima of T^*. Fig. 4b shows $P1$ is taken from the base of the non-monotonic temperature profile at approximately $t^* = 0.18$, then evenly spaced between $0.18 < t^* < 1$; therefore, the corresponding locations are applying to P^*. Discrepancies between the present uRANS model and the Gouda study [27] can arise from various factors. From a numerical perspective, differences in the setup, solvers, and accuracy between the turbulence models can lead to slight discrepancies in results. Disparities compared to experimental values could be attributed to the model's inaccuracy compared to a physical experiment. Furthermore, it could stem from the equipment and methods used to calculate the variables. Gouda's experiment relies solely on pressure readings to calculate the temperature, which uses an inverse method based on the ideal gas law ($T = PVT_0/P_0V_0$) with no additional methods for validation [27]. Given the minor variations in pressure and temperature compared to the reference data [27], the present numerical model accurately predicts the parameters in the present liquid piston-driven expansion process.

3. Results

The results in this section are split into baseline (no porous media inserts) and porous media insert cases. Baseline cases provide benchmark results on the temperature distribution and overall process efficiency while investigating the thermal effects of different boundary conditions on the cylinder wall. The porous media cases further explore the flow physics and how their inclusion affects heat transfer and efficiency.

3.1. Baseline cases (no porous media)

The wall thermal boundary conditions imposed for the baseline cases are either Case (i), a constant temperature set to 298 K, or Case

Table 2
Relative error analysis of validation study between present uRANS model and reference data from Gouda et al. experimental and LES work [27].

Data point	P^*		T^*	
	Experiment [27]	LES [27]	Experiment [27]	LES [27]
$P1$	−0.94%	−0.37%	+0.49%	−1.21%
$P2$	−1.87%	−1.21%	−0.07%	−1.65%
$P3$	−2.12%	−1.87%	−0.27%	−1.61%
$P4$	−2.24%	−1.70%	−0.91%	−1.40%

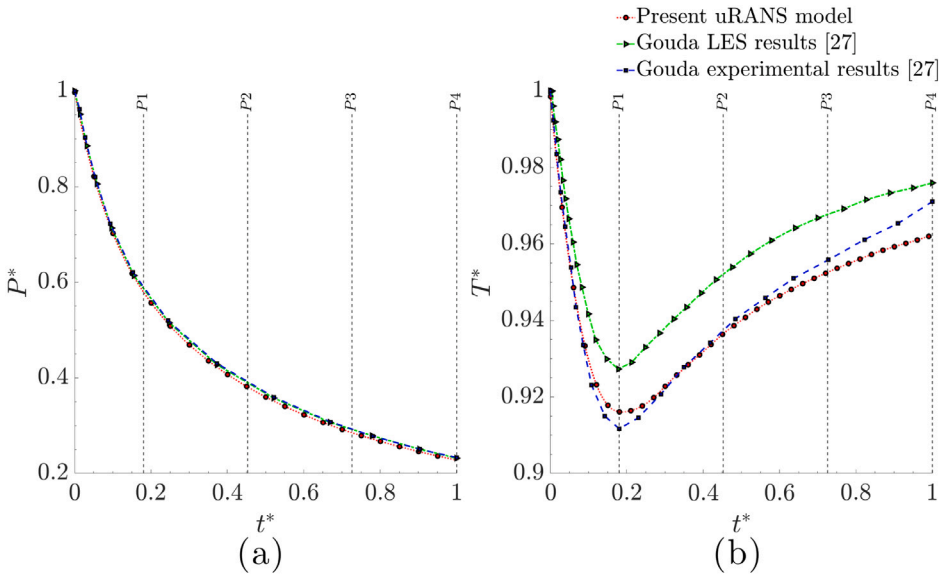

Fig. 4. Comparisons of time-dependent (a) normalised pressure (P^*) and (b) temperature (T^*) from present uRANS model against LES and experimental data from Gouda et al. [27].

(ii), an adiabatic wall condition. Results are presented at different radial (X) and axial (Y) positions.

3.1.1. Case (i): Constant wall temperature boundary condition

Using a constant temperature for the wall's thermal boundary condition creates a temperature gradient in the radial direction, providing a constant cooling effect and aiding in reducing the air temperature as it expands. The expanding volume increases the surface area for heat transfer, further assisting in the reduction of the air temperature, and the resulting thermal effects of the wall lead to a final T_{ave} of 285 K (Fig. 5). As the temperature decreases more rapidly, so does the pressure, and the increased transfer of work leads to an expansion duration of approximately 2.91 s.

A density increase occurs in the expanding air towards the liquid–gas interface; consequently, this 12.2% increase in density results in a further temperature reduction from the bulk temperature to 263 K. Fig. 5 displays a significant temperature gradient developing, leading to a non-uniform temperature distribution throughout the air mass fraction; where $\partial T/\partial y$ creates further variations in density which disrupt the flow field. Furthermore, the constant lower wall temperature enables $\partial T/\partial x$ to facilitate convection currents, with the higher-temperature air rising through the centre of the cylinder and the cooler, denser air descending at the walls. Fig. 6 displays this flow behaviour in more detail, with time-dependent behaviour of the axisymmetric convection currents increasing in magnitude throughout the expansion process. This effect is simplified by the Boussinesq approximation, which assumes that density changes only affect the buoyancy forces rather than the entire flow. The convection type can be established by calculating the Richardson number (Ri), which is the ratio of buoyancy forces to flow shear, which is given as [43]: $\mathrm{Ri} = (g\beta(T_{hot} - T_{cold})L)/\bar{u}_y^2$, with β being the air's thermal expansion coefficient, which is equal to $1/T$ for an ideal gas, L the characteristic length, in this case is the cylinder's diameter and $\bar{u}_y$ is the mean axial velocity.

The parameters during Case (i) result in a $\mathrm{Ri} > 1$, indicating natural convection; therefore, to establish the flow regime, we can calculate the Rayleigh Number (Ra) as a function of the Grashof (Gr) and Prandtl (Pr) numbers [44]: $\mathrm{Ra} = \mathrm{Gr}\times\mathrm{Pr} = (g\beta(T_{wall} - T_f)D^3)/(\nu\alpha)$, with ν and α as the kinematic viscosity and thermal diffusivity, respectively. The average Gr in the air mass fraction is $O(10^7)$ with its maximum in $O(10^8)$, demonstrating that buoyancy forces are significantly stronger than viscous forces (Fig. 6). The result is an average Ra of the same order, exhibiting a turbulent natural convection regime [45]. A minimum local Ra of $O(10^5)$ is encountered at the top end of the cylinder, which falls into the transitional regime; in this region, unsteady shearing motions are created in the fluid layers, resulting in roll-ups at the wall with approximately a 3% density fluctuation in these locations.

The unsteady flow features are enhanced by sustained convection; to ascertain the level of convective heat transfer, the volume-averaged Nusselt number is calculated. The subsequent correlation by Nagendra et al. [46] is applied to determine the average Nusselt number (Nu) as a function of Ra and the cylinder dimensions; the following correlation is valid for vertical cylinders with uniform heat flux: $\mathrm{Nu}_D = A\left(\mathrm{Ra}_D D/L\right)^B$, where A and B are constants of 0.6 and 0.25, respectively [46]. The result is high convective heat transfer in the air mass fraction, with a volume-average Nu value of 19.6. The non-monotonic time-dependent behaviour is a result of the $\Delta T \rightarrow 0$ then reversing so $T_{air} < T_{wall}$ in the final stages (Fig. 7). Throughout the expansion process, a temperature gradient is always present due to the constant temperature of the cylinder wall, which promotes convection as ΔT decreases between the air and the cylinder wall. When combined with the increasing surface area for heat transfer, the gradient helps maintain an energy imbalance, along with the previously mentioned

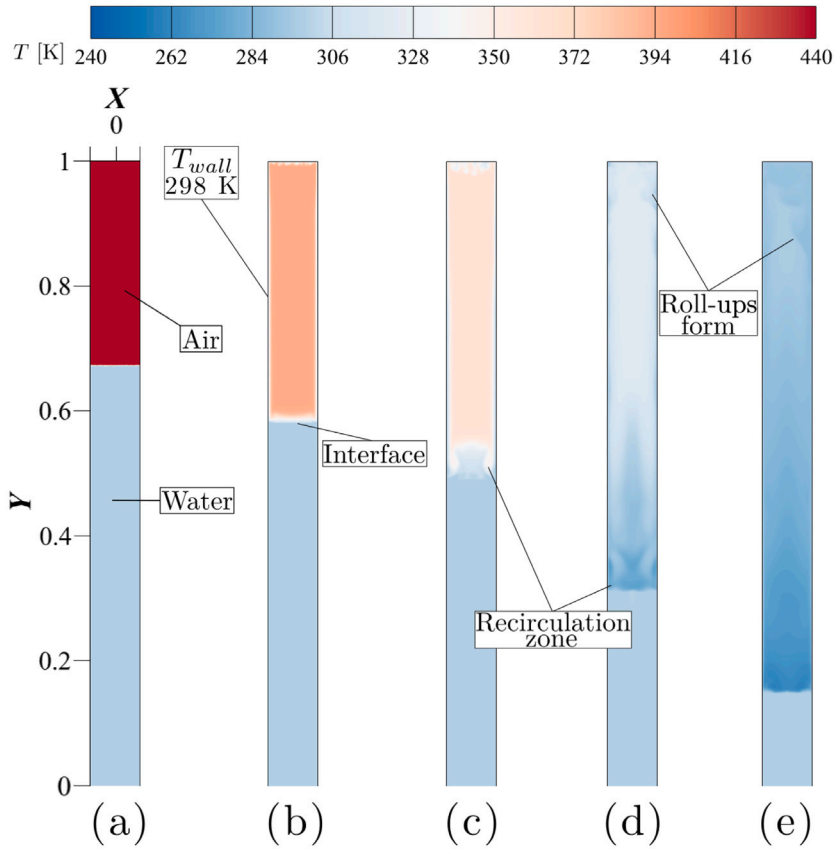

Fig. 5. Instantaneous temperature distribution of Case (i) using constant wall temperature boundary condition at: (a) 0 s, (b) 0.5 s, (c) 1 s, (d) 2 s, (e) 2.91 s.

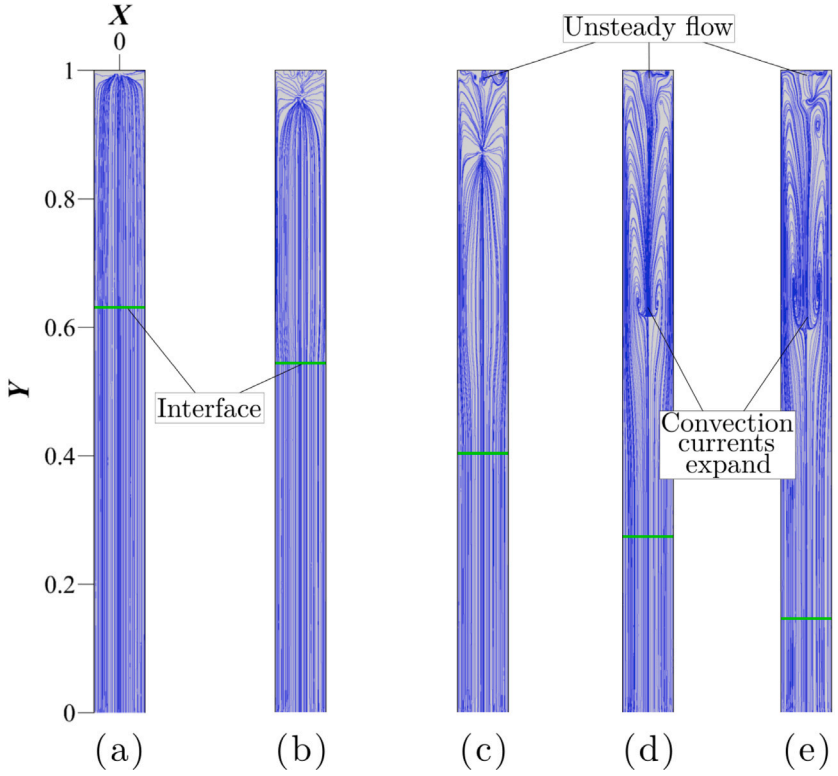

Fig. 6. Flow streamlines of $\langle \vec{u} \rangle$ through LPGC/E centre plane of Case (i) at: (a) 0 s, (b) 0.5 s, (c) 1 s, (d) 2 s, (e) 2.91 s.

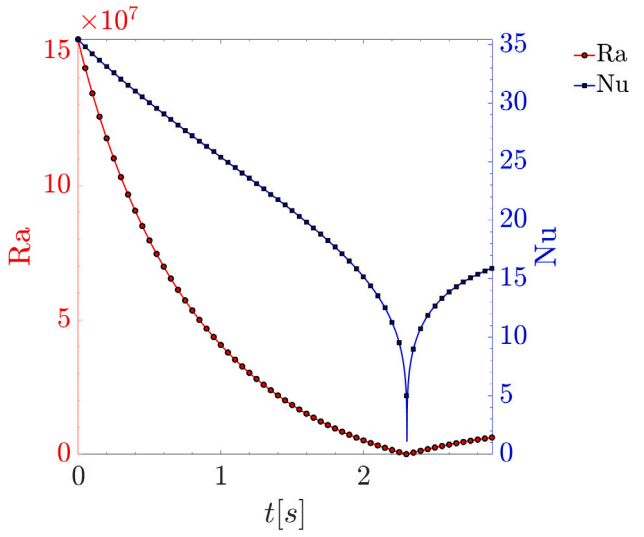

Fig. 7. Time-dependent behaviour of volume-averaged Ra and Nu in air mass fraction throughout Case (i) using constant wall temperature boundary condition.

factors, contributing to the expansion of convection currents within the LPGC/E, leading to an unsteady flow. These flow features are similar to those observed in the Gouda et al. [27] study; their LES work exhibits a regime transition as the air expands at lower temperatures.

Gouda et al. [27] report an 89.7% expansion efficiency for a fast expansion stroke using a constant wall temperature (300 K); however, the difference between the studies lies in the fact that their working fluid is in thermal equilibrium with the surroundings prior to expansion. The result is an expansion stroke recording a T_{ave} of approximately 262 K before recovering, with the heat transfer from the surroundings then allowing the gas to reattain a near-thermal equilibrium state. This recorded temperature represents the volume average; therefore, the temperatures experienced inside the chamber may be significantly lower, especially when approaching the liquid–gas interface, as observed in Case (i). In the present study, adopting equivalent thermal boundary conditions yields a significantly different outcome, with a W_{out} achieved through the expansion process of 1.77 kJ, resulting in an expansion process efficiency of 79.7%.

3.1.2. Case (ii): Adiabatic wall boundary conditions

By changing the cylinder wall boundary conditions to adiabatic, the internal energy change is entirely due to the work done by the expanding gas, resulting in an expansion stroke of approximately 3.1 s. Applying this thermal boundary condition results in a general temperature reduction when completing an expansion stroke; however, at the liquid–gas interface, a localised reduction is observed from the bulk temperature to 276 K; Fig. 8 provides more detail on this. A temperature recovery occurs in the water mass fraction due to its higher specific heat, producing minimal temperature changes (Fig. 9a). In the air mass fraction, the temperature decrease causes a 7.31% density increase; this relationship is consistent with the ideal gas behaviour ($\rho(y) \propto T^{-1}(y)$). A further density increase is observed at the interface, which is influenced by the interfacial tension of the water, diffusion processes and the density gradient in both phases. These factors contribute to a smooth transition rather than a sharp increase in density despite the vast density difference between the two phases. As the air expands and its density decreases, the resulting $\Delta\rho$ across the liquid–gas interface increases, which enhances the interfacial transition zone and accompanying temperature gradients, as governed by thermodynamic and diffusive transport processes. Throughout the expansion, a fully developed turbulent flow profile materialises by the process conclusion (t_e), with approximately an 11% increase in time-averaged mean axial velocity ($\langle\bar{u}\rangle$) towards the interface (Fig. 9b). During the Gouda case [27], the same interface characteristics are present in the LES modelling. Subsequently, the above represents how the contained fluid mechanics behave without external thermal influences.

Adopting the adiabatic boundary conditions improves the available work within the expansion process to 1.83 kJ, compared to 1.77 kJ in Case (i). Additionally, the E_s from the compressed air is 2.22 kJ for both baseline cases; the E_s/W_{out} ratio improves, resulting in an increase in expansion efficiency to 82.4%. Therefore, adiabatic walls are applied on the cylinder during porous insert cases to maximise efficiency and establish the influence of the porous inserts on the expansion process.

3.2. Porous media cases

Porous media inserts are essential for delivering a near-isothermal process by enhancing heat transfer with the working gas during compression [17]. Furthermore, as the LPGC/E is a combined unit, the inserts will also be present during expansion. This section analyses two types of porous media and different thermal boundary conditions (Section 2.2) to investigate the optimised configuration for an expansion process. Localised flow disturbances are captured, and their impact on heat transfer is explored using a 3-D porous media arrangement as opposed to a representative elementary volume (REV).

3.2.1. Case (iii): Porous media at 298 K

In Case (iii), as the cylinder wall is adiabatic, any heat transfer that occurs is solely through the porous inserts. The initial insert temperature is 298 K, creating a thermal imbalance between the insert and the surrounding air, which drives heat transfer from the high-temperature air to the cooler inserts (Fig. 10). A temperature gradient is formed due to the inclusion of the inserts, resulting in a density increase in the porous region; consequently, the density variations are intensified as the air vacates the porous region and enters the cylinder's non-porous region.

As the denser air is positioned above the lighter air, the density differential and the fluid's stability can be characterised using the Atwood number (At) [47]: $\mathrm{At} = (\rho_1 - \rho_2)/(\rho_1 + \rho_2)$, where ρ_1 is assigned as density inside the porous region and ρ_2 as outside. Initially, as t approaches 1 s, $\mathrm{At} > 0$ signifying density stratification and the potential for fluid flow instabilities [48]. The density stratification is enhanced by a channelling effect produced by the inserts, which increases $\langle\bar{u}_y\rangle$ by 8.2%, creating a jet-like feature that disperses cooler, higher-density air into the non-porous region. When $t > 0.5$ s, the axial velocity gradient created by the exiting air mixes with the stagnant air outside the porous region, producing an unsteady shearing effect (Fig. 11a).

Shear flow instabilities are known to arise downstream of a sudden axisymmetric expansion [49,50], i.e., as the air exits the porous region. In this case, the ratio between the insert's pore size and cylinder diameter is approximately 0.06, resulting in a significant expansion when entering the cylinder's non-porous region. When coupled with velocity and density gradients, the sudden expansion induces shear-flow instabilities – specifically Kelvin–Helmholtz (K-H) instability – in the region between the exit of the porous inserts (0.8 m) and the cylinder wall. Fig. 12 presents this phenomenon in more detail, highlighting how influential the early stages of expansion ($0.25 < t < 1$ s) are on the developing flow within the non-porous region in the latter stages of the process. As $\Delta\rho$ increases between porous and non-porous regions, in conjunction with the $\langle\bar{u}_y\rangle$ channelling effect, the axisymmetric instabilities grow in magnitude. The shear instabilities are at their largest when $\langle\bar{u}_y\rangle$ peaks at $t = 1$ s (Fig. 12d). However, as the process advances between $1.25 < t < 1.5$ s, the channelling effect subsides and the flow begins to deform asymmetrically, breaking away from the porous region as the air expands (Figs. 12d and e), producing the anisotropic flow prominent in Figs. 10c through 10e. At this point,

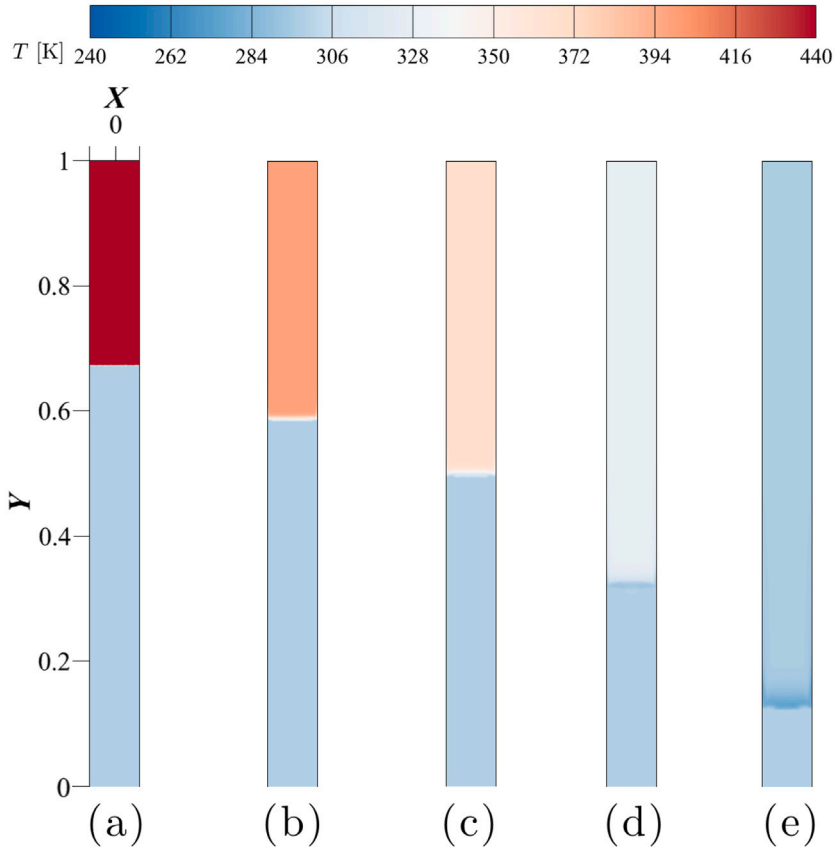

Fig. 8. Instantaneous temperature distribution of Case (ii) using adiabatic wall boundary condition at: (a) 0 s, (b) 0.5 s, (c) 1 s, (d) 2 s, (e) 3.08 s.

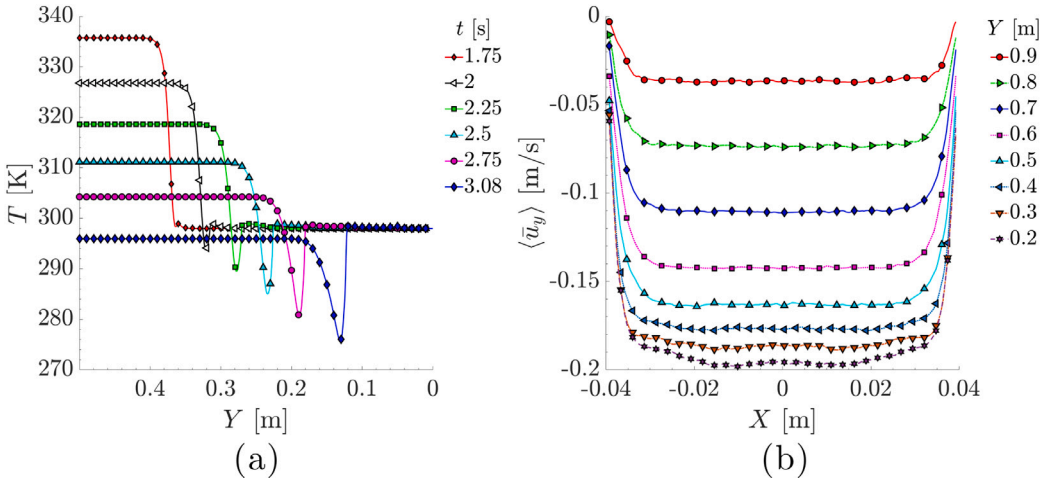

Fig. 9. Axial distribution of (a) temperature focusing on liquid–gas interface and (b) radial distribution of time-averaged axial velocity ($\langle \bar{u} \rangle$) within air mass fraction during Case (ii).

$t > 1.5$ s, porous media's impact on the flow becomes less influential as they approach thermal equilibrium with the air, decreasing $\Delta\rho$; together with a significant decrease in $\langle \bar{u}_y \rangle$. As the process concludes, a 14.5% reduction in $\langle \bar{u}_y \rangle$ occurs from u_0 (Fig. 11b), lessening the channelling effect, resulting in further mixing as a function of density variations as the air continues to expand through the non-porous region.

Initially, vorticity production is driven by the change in density (Fig. 13a and b) and velocity when the air vacates the porous region and mixes in the non-porous region. Further density changes occur in the non-porous region as a result of the air volume increasing and the formation of a further axial temperature gradient. These factors lead to turbulent effects developing in the non-porous region while being severely reduced within the porous region. Consequently, this continuous cycle of temperature and density changes continues throughout the expansion stroke, resulting in higher areas of vorticity. In the expansion's final stages, as $\Delta T \rightarrow 0$ between air and inserts, the density changes and mixing are suppressed.

The increased heat transfer and internal energy reduction negatively impact the expansion process; as such, the average heat transfer coefficients (HTC) at t_e for the parallel plates and metal foam are 195.98 and 260.29 W/m^2·K, respectively. These HTC values are consistent with those of our previous compression work [17]. As the process concludes,

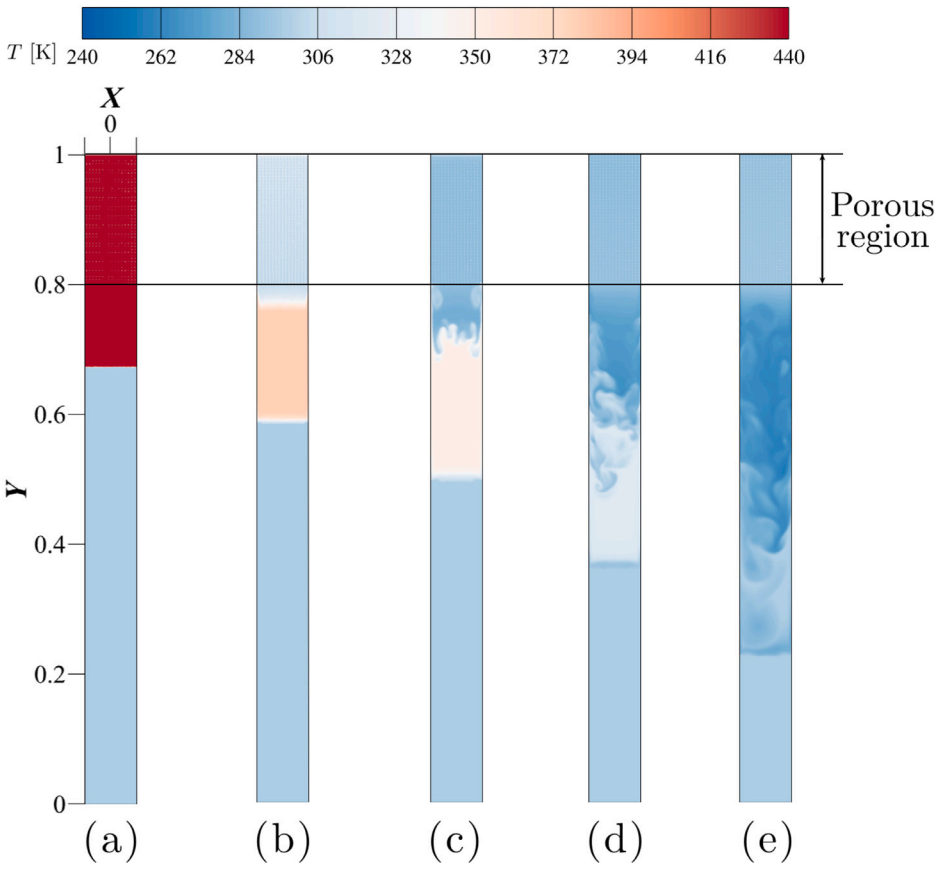

Fig. 10. Instantaneous temperature contours of Case (iii) fast expansion process at: (a) 0 s, (b) 0.5 s, (c) 1 s, (d) 1.75 s, (e) 2.65 s.

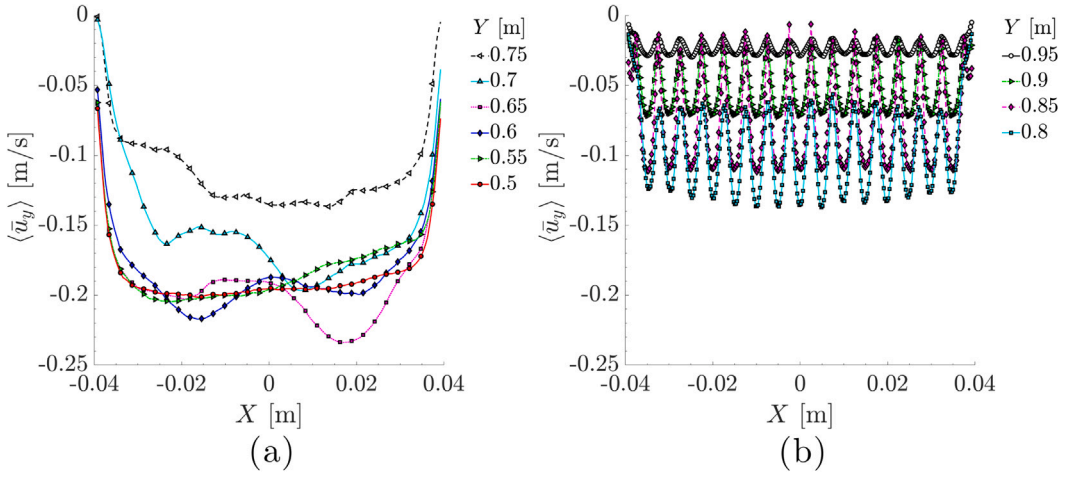

Fig. 11. Radial distribution of $\langle \bar{u}_y \rangle$ component in air mass fraction during Case (iii) fast expansion stroke; data taken from (a) outside porous region and (b) inside porous region.

a final T_{ave} of 281 K occurs, which represents a 15 K reduction from Case (ii); furthermore, the interface temperature during Case (iii) is approximately the same as T_{ave}; this is an effect of the density variations throughout the cylinder (Figs. 10 and 13b). With the inserts present, a reduced expansion stroke of 2.65 s occurs due to increased heat transfer. According to the ideal gas law, the time required to reach the final pressure decreases as the air temperature decreases.

Using the porous insert when $T_{plate} < T_{air}$ reduces the expansion efficiency by 5%–6% from the baseline to 77% for the parallel plates and 76% for the metal foam. The efficiency decrease occurs due to the reduction in mechanical work performed during the expansion process, with values of 1.52 kJ for the parallel plates and 1.6 kJ for the metal foam achieved, compared to 1.83 kJ in Case (i). A reduction in process efficiency further demonstrates that heat within the cylinder must be conserved; therefore, one option is to apply a heat source when a fast expansion process is required. Alternatively, greater control over the liquid piston allows for varied outflow conditions, which increases the expansion duration and mitigates temperature reduction. Both methods are important in creating a near-isothermal process.

In a protracted scenario, the adverse effects of the low-temperature inserts are amplified when the flow rate is reduced to 5 l/min. The density variations observed during the fast expansion are intensified,

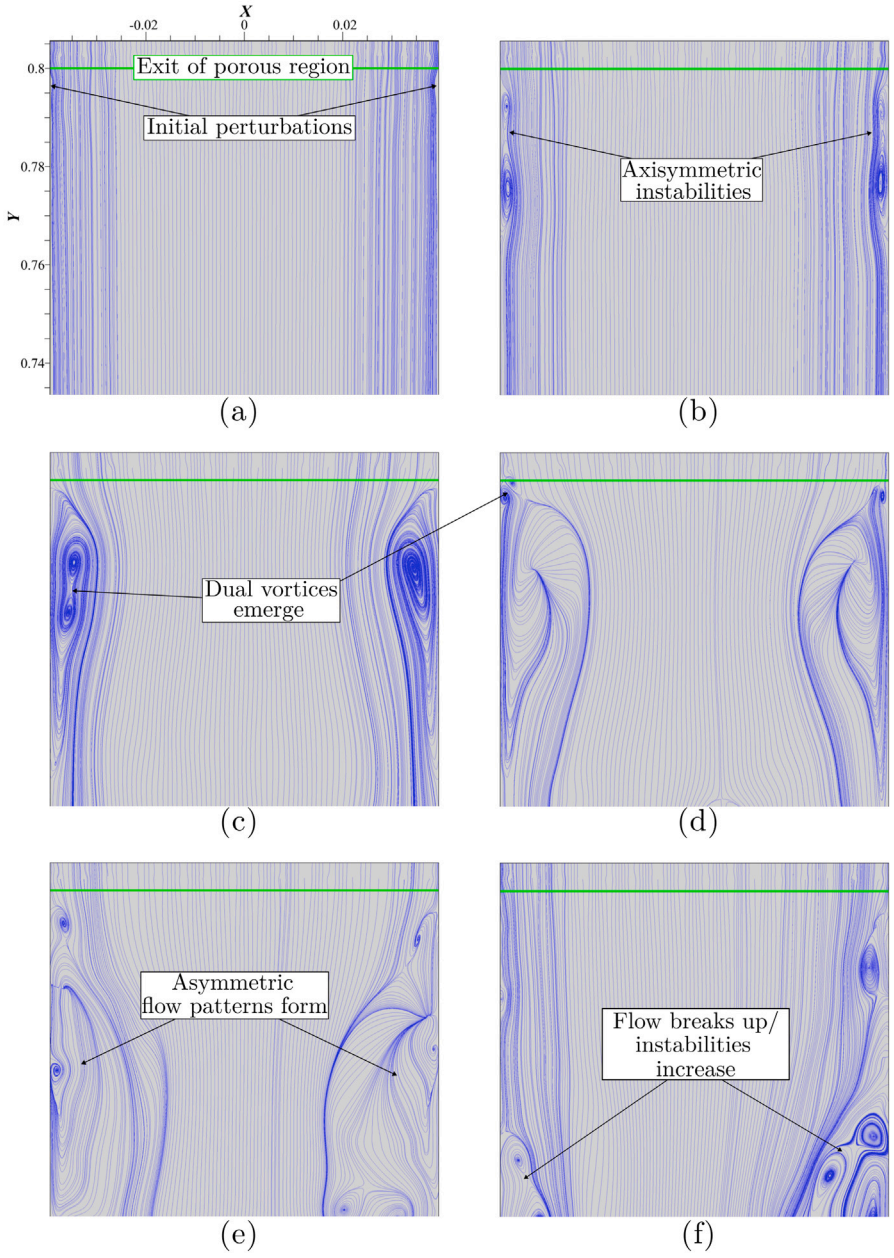

Fig. 12. Shear-layer instabilities developing downstream of Case (iii) porous region when expanded into non-porous region. Instantaneous velocity streamlines are plotted for different time steps during Case (iii): (a) 0.25 s, (b) 0.5 s, (c) 0.75 s, (d) 1 s, (e) 1.25 s and (f) 1.5 s.

further increasing the vorticity; these changes in density and vorticity cause the air to recirculate as it exits the porous insert. The deviations increase over time, causing the air to re-enter the porous region, and this cycle repeats itself throughout the expansion process. Due to the extended period, the air interacts with the porous inserts, allowing additional time for heat transfer, which reduces the air temperature and, consequently, the expansion efficiency.

The extended process concludes with an T_{ave} of 270.75 K with a minimum value of 254.39 K at the interface—the most significant temperature decrease of all the expansion cases. The insert temperature increases slightly to 300 K, with the air inside the porous region being higher than in the fast expansion at 294.57 K, which reduces the ΔT and lowers the average HTC to 15.68 W/m^2·K. Consequently, the output work performed during the slower expansion process is reduced to 1.52 kJ, further reducing the efficiency of the expansion process to 72.1% when a 26-second expansion stroke is completed with the metal foam geometry. Reducing the outlet flow rate with this thermal arrangement establishes that the flow rate must be significantly decreased to achieve a near-isothermal process. However, if a prolonged expansion stroke cannot ensue, it demonstrates the requirement for a heat source to achieve a near-isothermal process.

3.2.2. Case (iv): Porous media at 440 K

Increasing the temperature imposed on the inserts provides insight into how the inserts perform over multiple cycles, as their temperature will increase over time due to prolonged exposure to high-temperature air. An alternative scenario involves adding a heat source to the expansion process, which can facilitate a near-isothermal process. Initially, within the porous region, the air and insert are in thermal equilibrium; but, as the air cools, the accumulated heat from previous strokes is released back into the air. The sustained thermal energy levels provide a more efficient resource for mechanical work during expansion, thereby improving the expansion efficiency. The elevated insert temperature yields average HTC values of −1.39 and −1.25 W/m^2·K for

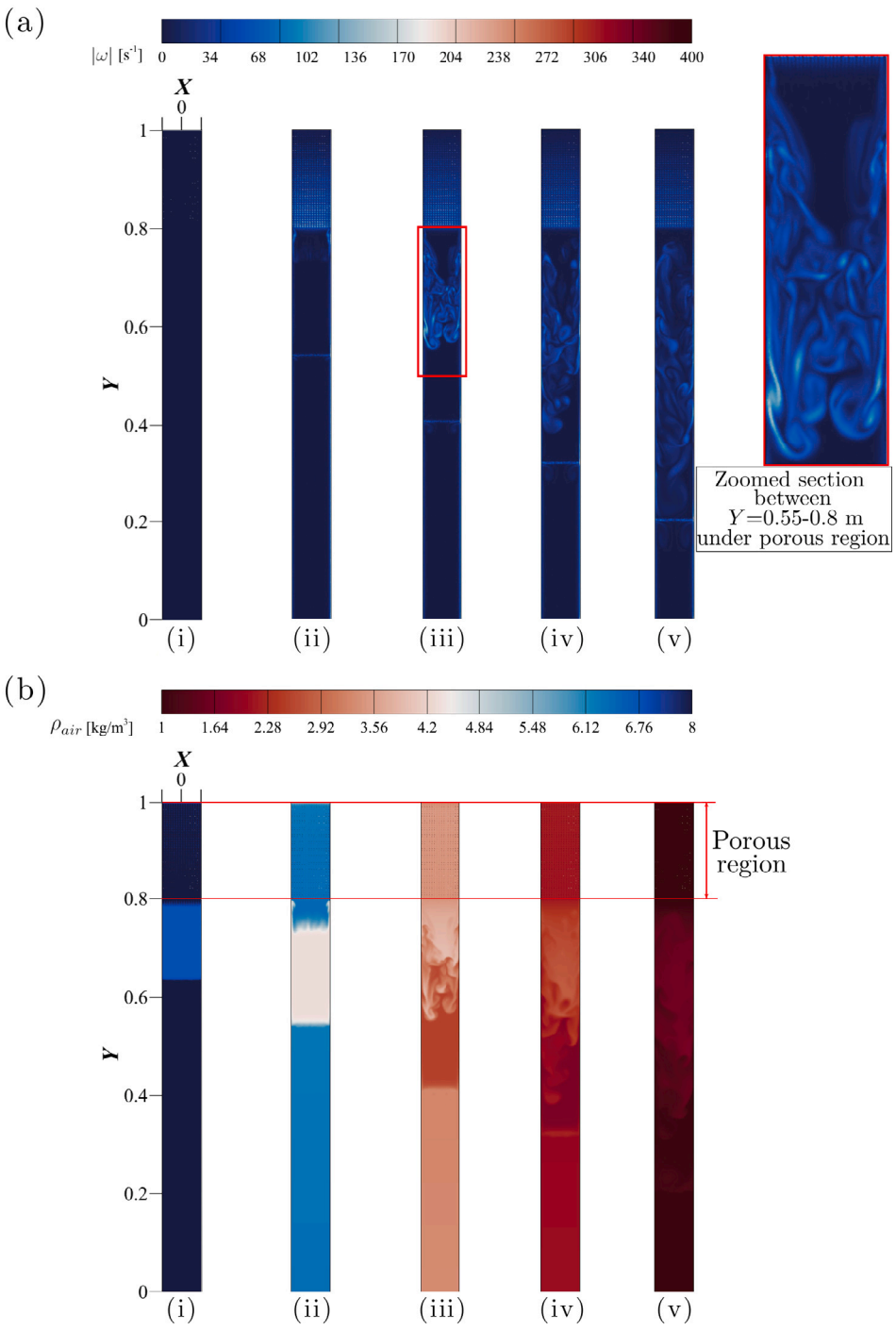

Fig. 13. Instantaneous (a) vorticity magnitude and (b) air density progression during Case (iii) fast expansion stroke at: (i) 0 s, (ii) 0.5 s, (iii) 1 s, (iv) 1.75 s and (v) 2.65 s.

the parallel plates and metal foam, respectively, indicating that heat is being transferred from the plates to the cooling air. A larger SA/V ratio for the metal foam is attributed to the higher HTC value between parallel plates and the metal foam. Compared to Case (iii), the addition of sustained thermal energy increases the final T_{ave} to approximately 343 K, which enhances the W_{out} to 1.83 kJ. In Case (iv), W_{out} is the same value as in the adiabatic baseline case; however, a 6% improvement is achieved over the adiabatic baseline case, resulting in approximately 88% as a consequence of the increased available work. W_{out} (Eq. (13)) is improved from the higher temperature as an increase in final air volume is encountered to reach the required final pressure. Additionally, E_s is reduced from the adiabatic case due to the inserts decreasing the initial air volume (Eq. (14)), thereby improving the W_{out}/E_s ratio. Increasing the thermal energy significantly alters the flow physics compared to Case (iii). No density or temperature fluctuations are present to disturb the flow, resulting in gradual changes ($T^{-1} \propto \rho$) as the process approaches its conclusion (Fig. 14). Furthermore, as the volume density decreases, $\partial\rho/\partial y$ increases towards the interface from the higher temperature in the porous region, which significantly reduces the density in that region. The density increase from the insert exit approaching the interface is 46%, with a further 8% increase at the interface where the fluid transitions from α_a to α_w. Similar to the adiabatic baseline conditions (Case (i)), the boundary layer remains attached to the wall in the non-porous region, resulting in a fully

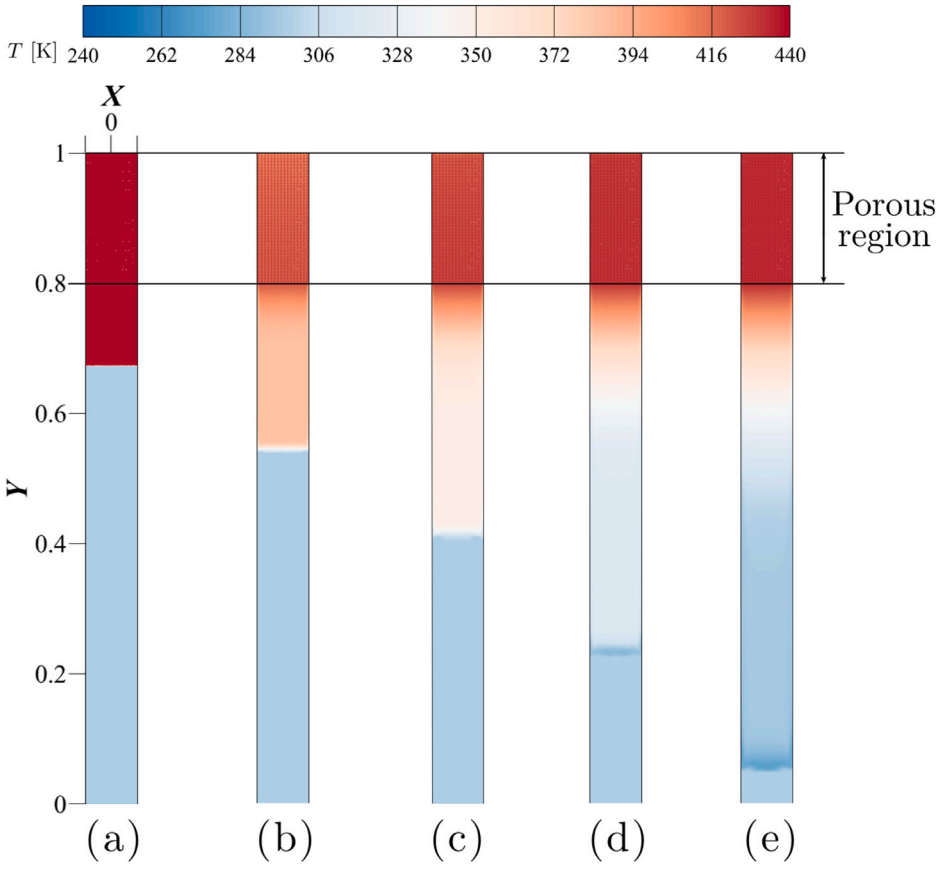

Fig. 14. Instantaneous temperature contours of Case (iv) fast expansion stroke at: (a) 0 s, (b) 0.75 s, (a) 1.5 s, (b) 2.5 s and (e) 3.49 s.

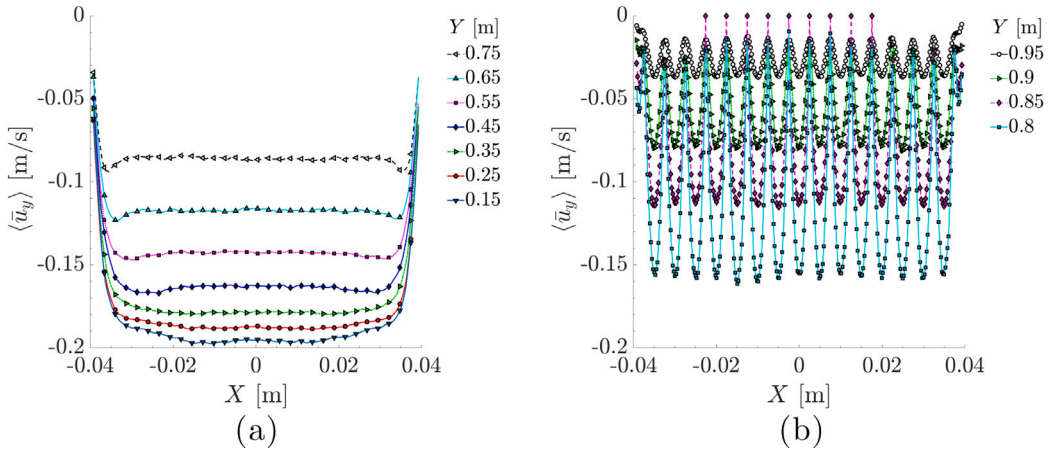

Fig. 15. Radial distribution of $\langle \bar{u}_y \rangle$ component in air mass fraction during Case (iv) fast expansion stroke; data taken from (a) outside porous region and (b) inside porous region.

developed turbulent flow throughout (Fig. 15a). In the porous region, the channelling effect boosts the intrinsic velocity by 16% within 0.25 s, followed by a 56% reduction by the process conclusion (Fig. 15b). However, the elevated air temperature diminishes the sudden density changes. Using the Atwood number to assess the fluid flow stability, an At < 0 is encountered, eliminating the unsteady flow features observed in Case (iii).

Once more, the mass outflow rate is reduced to 5 l/min, and a 35-second expansion stroke occurs. This protracted expansion increases T_{ave} slightly to approximately 346 K, resulting in an average HTC of −0.11 W/m^2·K, which is close to reversing the direction of heat transfer. A limitation of the CHT method is that the solver settings allow the plates to cool during contact with the cooling air. While this is suitable for a prolonged expansion stroke with heat accumulated in the inserts, it does not align well with the heat source scenario, as a heat source will continue to generate heat and remain unaffected by the decreasing air temperature. With prolonged exposure to the high-temperature inserts, the expansion efficiency improves by 0.5%, suggesting that porous inserts at higher temperatures are better suited for shorter expansion strokes.

4. Conclusion

This study focused on the fluid dynamics and heat transfer during an expansion process using a liquid piston, aiming to improve the efficiency of the expansion process. The importance of maintaining air temperature during the expansion process is evident throughout; this is demonstrated in the baseline cases, where efficiency is highest in the adiabatic wall cylinder (Case (ii)), where no heat transfer occurs. Additionally, the high-temperature inserts (Case (iv)) yield the highest process efficiency, indicating that efficiency improves after multiple expansion strokes. Alternatively, this efficiency improvement could be achieved by applying a heat source to produce a near-isothermal process within the LPGC/E, though this approach may be challenging to implement.

In cases where a source applies a temperature lower than the initial air temperature, such as an uninsulated cylinder wall (Case (i)) or cold plates (Case (iii)), various turbulent flow features emerge during the expansion process. Turbulent features have been proven to increase heat transfer within systems; yet, during the expansion process, heat transfer that decreases the air temperature needs to be minimised. In the case of constant wall temperature and porous media, where lower temperatures are applied, the expansion process efficiency decreases to 79.7% and 72.2%, respectively—further highlighting the need for a near-isothermal expansion process.

The duration of the expansion stroke is also a key factor; when using high temperatures pre-expansion, shorter expansion strokes perform better than a protracted process. As the insert temperature increases after multiple strokes – or through the use of a heat source – this brings the system closer to thermal equilibrium, resulting in significant improvements in process efficiency. By averaging the values for both thermal conditions, the efficiency is approximately 82%, which is equal to the efficiency of the cases with no porous inserts. Using shorter strokes, the metallic insert method can generate higher efficiencies during compression [17], and the expansion efficiency can be maintained over multiple cycles, providing a higher component-level RTE.

The limitations of this study come from two main factors, one being from a computational standpoint and the other from an operational perspective. From a computational perspective, the model and geometry use various assumptions to simplify the arrangement, i.e., the whole bottom LPGC/E face as an outlet boundary condition. In a case more aligned with a real-world application, an outlet pipe similar to a physical component should be added. Having a 6 to 13 mm outlet in comparison to 79 mm will change how the flow functions within the water mass fraction. Also, the outlet is designated as a constant flow rate; yet, operationally, this would be imposed on a ramping scale. Therefore, in future work, a non-linear outflow should be applied to represent a physical application accurately.

From an operational setup, the implementation of the high-temperature heat source required to bring the system into thermal equilibrium will pose challenges to its successful execution. Applying a heat source to other parts of the LPGC/E, i.e., cylinder wall, may be better suited when employing this method to achieve a near-isothermal expansion. Furthermore, when encountering the high temperatures selected in this investigation, the multiphase system will undergo evaporation and condensation. Factoring such phenomena into the numerical model will provide a sounder understanding of how each will affect the overall LPGC/E performance.

For future work, we aim to investigate fluid physics further using higher-fidelity numerical methods. Methods such as LES or DNS can provide more in-depth insight into the intricate details. The phenomena observed in the baseline and porous media cases, such as the instabilities and the liquid–gas interface, can be analysed in greater detail. However, such methods come at a cost due to the computational capacity required to run such simulations.

CRediT authorship contribution statement

Lee Haney: Writing – review & editing, Writing – original draft, Visualization, Validation, Software, Project administration, Methodology, Investigation, Formal analysis, Data curation, Conceptualization. **Robert Prosser:** Writing – review & editing, Visualization, Supervision, Project administration, Funding acquisition, Conceptualization. **Alexander Lanzon:** Writing – review & editing, Supervision, Resources, Project administration, Funding acquisition. **Yasser Mahmoudi:** Writing – review & editing, Supervision, Software, Project administration, Funding acquisition, Conceptualization.

Declaration of competing interest

The authors declare the following financial interests/personal relationships which may be considered as potential competing interests: Yasser Mahmoudi Larimi reports financial support was provided by Engineering and Physical Sciences Research Council. If there are other authors, they declare that they have no known competing financial interests or personal relationships that could have appeared to influence the work reported in this paper.

Acknowledgements

This work was supported by the UK Engineering and Physical Sciences Research Council (EPSRC) [grant number EP/Y017471/1]. The authors would like to acknowledge the assistance given by Research IT and the use of the Computational Shared Facility at The University of Manchester.

Data availability

Data will be made available on request.

References

[1] International Energy Agency, Global Energy Review 2025, 2025, URL: https://iea.blob.core.windows.net/assets/909b7120-1cbd-439a-a9da-e971a4419977/GlobalEnergyReview2025.pdf.
[2] S.D. Garvey, A.J. Pimm, Compressed air energy storage (CAES), 2022, pp. 117–140, http://dx.doi.org/10.1016/b978-0-12-824510-1.00031-3, Storing Energy (Second Edition) with Special Reference to Renewable Energy Sources.
[3] S. Donadei, G.-S. Schneider, Compressed air energy storage, Elsevier EBooks (2022) 141–156, http://dx.doi.org/10.1016/b978-0-12-824510-1.00034-9.
[4] M. Budt, D. Wolf, R. Span, J. Yan, A review on compressed air energy storage: Basic principles, past milestones and recent developments, Appl. Energy 170 (2016) 250–268, http://dx.doi.org/10.1016/j.apenergy.2016.02.108.
[5] D.R. Hounslow, W. Grindley, R.M. Loughlin, J. Daly, The development of a combustion system for a 110 MW CAES plant, J. Eng. Gas Turbines Power 120 (1998) 875–883, http://dx.doi.org/10.1115/1.2818482.
[6] F. Crotogino, K.U. Mohmeyer, R. Scharf, Huntorf CAES: More than 20 years of successful operation, in: SMRI Spring Meeting, Orlando, USA, Solution Mining Research Institute, 2001, pp. 351–362.
[7] E. Barbour, D.L. Pottie, Adiabatic compressed air energy storage technology, Joule 5 (2021) 1914–1920, http://dx.doi.org/10.1016/j.joule.2021.07.009.
[8] L. Geissbühler, V. Becattini, G. Zanganeh, S. Zavattoni, M. Barbato, A. Haselbacher, A. Steinfeld, Pilot-scale demonstration of advanced adiabatic compressed air energy storage, Part 1: Plant description and tests with sensible thermal-energy storage, J. Energy Storage 17 (2018) 129–139, http://dx.doi.org/10.1016/j.est.2018.02.004.
[9] E. Barbour, D. Mignard, Y. Ding, Y. Li, Adiabatic compressed air energy storage with packed bed thermal energy storage, Appl. Energy 155 (2015) 804–815, http://dx.doi.org/10.1016/j.apenergy.2015.06.019.
[10] E.R. Barbour, D.L. Pottie, P. Eames, Why is adiabatic compressed air energy storage yet to become a viable energy storage option? IScience 24 (2021) 102440, http://dx.doi.org/10.1016/j.isci.2021.102440.
[11] X. Zhang, H. Chen, Y. Xu, X. Zhou, H. Guo, Isothermal compressed air energy storage, in: Compressed Air Energy Storage: Types, systems and applications, The Institution of Engineering and Technology, 2021, pp. 29–54, http://dx.doi.org/10.1049/pbpo184e_ch3.
[12] M. Stewart, Compressor fundamentals, Surf. Prod. Oper. IV (2019) 457–525, http://dx.doi.org/10.1016/b978-0-12-809895-0.00007-7.

[13] X. He, H. Wang, G. Ge, Y. Liu, Y. Zhang, Thermodynamic analysis of a hybrid system combining compressed air energy storage and pressurized water thermal energy storage, Appl. Therm. Eng. 229 (2023) 120568, http://dx.doi.org/10.1016/j.applthermaleng.2023.120568.

[14] Y. Zhang, P. Jin, H. Wang, X. Cai, X. Li, W. Zhang, H. Wang, R. Li, Design, analysis and optimisation of a novel adiabatic-isothermal CAES system with coupled stepped phase change energy storage unit, Appl. Therm. Eng. 256 (2024) 124091, http://dx.doi.org/10.1016/j.applthermaleng.2024.124091.

[15] R. Li, R. Tao, E. Yao, H. Zhang, Y. Niu, L. Ling, A. Yan, H. Wang, Decoupling heat-pressure potential energy of compressed air energy storage system: Using near-isothermal compressing and thermal energy storage, J. Energy Storage 63 (2023) 107017, http://dx.doi.org/10.1016/j.est.2023.107017.

[16] M. Khaljani, J. Harrison, D. Surplus, A. Murphy, P. Sapin, C. Markides, Y. Mahmoudi, A combined experimental and modelling investigation of an over-ground compressed-air energy storage system with a reversible liquid-piston gas compressor/expander, Energy Convers. Manage. 245 (2021) 114536, http://dx.doi.org/10.1016/j.enconman.2021.114536.

[17] L. Haney, R. Prosser, A. Lanzon, Y. Mahmoudi, Modelling of near isothermal liquid piston gas compressor employing porous media for compressed air energy storage systems, Int. J. Therm. Sci. 212 (2025) 109775, http://dx.doi.org/10.1016/j.ijthermalsci.2025.109775.

[18] Q. Zhou, D. Du, C. Lu, Q. He, W. Liu, A review of thermal energy storage in compressed air energy storage system, Energy 188 (2019) 115993, http://dx.doi.org/10.1016/j.energy.2019.115993.

[19] J.D. Van de Ven, P.Y. Li, Liquid piston gas compression, Appl. Energy 86 (2009) 2183–2191, http://dx.doi.org/10.1016/j.apenergy.2008.12.001.

[20] J. Wieberdink, P.Y. Li, T.W. Simon, J.D. Van de Ven, Effects of porous media insert on the efficiency and power density of a high pressure (210 bar) liquid piston air compressor/expander – an experimental study, Appl. Energy 212 (2018) 1025–1037, http://dx.doi.org/10.1016/j.apenergy.2017.12.093.

[21] M. Khaljani, A. Vennard, J. Harrison, D. Surplus, A. Murphy, Y. Mahmoudi, Experimental and modelling analysis of efficiency enhancement in a liquid piston gas compressor using metal plate inserts for compressed air energy storage application, J. Energy Storage 42 (2021) 103240, http://dx.doi.org/10.1016/j.est.2021.103240.

[22] N. Cerkovnik, V. Costa, A. Lopes, Modeling and parametric optimization of a liquid piston compressor with inner cooling tubes, Appl. Therm. Eng. 228 (2023) http://dx.doi.org/10.1016/j.applthermaleng.2023.120436, 120436–120436.

[23] A. Odukomaiya, A. Abu-Heiba, K.R. Gluesenkamp, O. Abdelaziz, R.K. Jackson, C. Daniel, S. Graham, A.M. Momen, Thermal analysis of near-isothermal compressed gas energy storage system, Appl. Energy 179 (2016) 948–960, http://dx.doi.org/10.1016/j.apenergy.2016.07.059.

[24] V.C. Patil, P.I. Ro, Experimental study of heat transfer enhancement in liquid piston compressor using aqueous foam, Appl. Therm. Eng. 164 (2020) http://dx.doi.org/10.1016/j.applthermaleng.2019.114441, https://doi.org/10.1007/s11242–019–01357–014441.

[25] M. Athadkar, S. Lorente, Reaching near-isothermal compression in liquid piston with PCM inserts, Appl. Therm. Eng. 274 (2025) http://dx.doi.org/10.1016/j.applthermaleng.2025.126758, 126758–126758.

[26] B. Yan, J. Wieberdink, F. Shirazi, P.Y. Li, T.W. Simon, J.D. Van de Ven, Experimental study of heat transfer enhancement in a liquid piston compressor/expander using porous media inserts, Appl. Energy 154 (2015) 40–50, http://dx.doi.org/10.1016/j.apenergy.2015.04.106.

[27] E.M. Gouda, T. Neu, M. Benaouicha, Y. Fan, A. Subrenat, L. Luo, Experimental and numerical investigation on the flow and heat transfer behaviors during a compression–cooling–expansion cycle using a liquid piston for compressed air energy storage, Energy 277 (2023) http://dx.doi.org/10.1016/j.energy.2023.127622, 127622–127622.

[28] H.M. Ali, T.-u. Rehman, M. Arıcı, Z. Said, B. Duraković, H.I. Mohammed, R. Kumar, M.K. Rathod, O. Buyukdagli, M. Teggar, Advances in thermal energy storage: Fundamentals and applications, Prog. Energy Combust. Sci. 100 (2024) 101109, http://dx.doi.org/10.1016/j.pecs.2023.101109.

[29] C. Zhao, M. Liu, G. Ni, J. Yan, Proposal design and thermodynamic optimization of an afterburning-type isothermal compressed air energy storage system integrated with molten salt thermal storage, J. Energy Storage 102 (2024) http://dx.doi.org/10.1016/j.est.2024.114163, 114163–114163.

[30] S. Fukusako, M. Takahashi, Free convection heat transfer of air-water layers in a horizontal cooled circular tube, Int. J. Heat Mass Transfer 34 (1991) 693–702, http://dx.doi.org/10.1016/0017-9310(91)90117-w.

[31] M. Specklin, M. Deligant, P. Sapin, M. Solis, M. Wagner, C.N. Markides, F. Bakir, Numerical study of a liquid-piston compressor system for hydrogen applications, Appl. Therm. Eng. 216 (2022) 118946, http://dx.doi.org/10.1016/j.applthermaleng.2022.118946.

[32] Y.J. Chae, J.I. Lee, Thermodynamic analysis of compressed and liquid carbon dioxide energy storage system integrated with steam cycle for flexible operation of thermal power plant, Energy Convers. Manage. 256 (2022) 115374, http://dx.doi.org/10.1016/j.enconman.2022.115374.

[33] C.-Y. Lee, H. Liu, L. Gao, J. Muehlbauer, Y. Hwang, R. Radermacher, Development of a near-isothermal transcritical CO_2 compression system with a liquid piston compressor, Appl. Therm. Eng. 261 (2024) 125108, http://dx.doi.org/10.1016/j.applthermaleng.2024.125108.

[34] Y. Liang, T. Lei, Y. Zhu, K. Ye, J. Wu, M. Dong, J. Lu, Energy consumption optimization of CO_2 capture and compression in natural gas combined cycle power plant through configuration modification and process integration, Appl. Therm. Eng. 255 (2024) http://dx.doi.org/10.1016/j.applthermaleng.2024.124019, 124019–124019.

[35] W. Sutherland, LII. The viscosity of gases and molecular force, Lond. Edinb. Dublin Philos. Mag. J. Sci. 36 (1893) 507–531, http://dx.doi.org/10.1080/14786449308620508.

[36] Siemens, Simcenter STAR-CCM+ user guide, 2024, URL: https://docs.sw.siemens.com/documentation/external/PL20200805113346338/en-US/userManual/userguide/html/index.html.

[37] H.K. Versteeg, W. Malalasekera, An Introduction to Computational Fluid Dynamics - The Finite Volume Method, second ed., Pearson Education, 2007.

[38] Y. Guo, Q. Wang, X. Liu, M. Zhang, X. Peng, Numerical analysis of the dynamic two-phase flow behaviour in the ionic liquid compressor for hydrogen refuelling stations, Appl. Therm. Eng. 219 (2022) 119607, http://dx.doi.org/10.1016/j.applthermaleng.2022.119607.

[39] A. Soldati, C. Marchioli, Differential form of conservation equations, Fluid Mech. Mech. Eng. (2024) 71–89, http://dx.doi.org/10.1007/978-3-031-53950-3_3.

[40] V. Guimet, D. Laurence, A linearised turbulent production in the k-ϵ model for engineering applications, in: Engineering Turbulence Modelling and Experiments 5, Elsevier Science Ltd, 2002, pp. 157–166, http://dx.doi.org/10.1016/B978-008044114-6/50014-4.

[41] C. Zhang, P.Y. Li, J.D. Van de Ven, T.W. Simon, Design analysis of a liquid-piston compression chamber with application to compressed air energy storage, Appl. Therm. Eng. 101 (2016) 704–709, http://dx.doi.org/10.1016/j.applthermaleng.2016.01.082.

[42] F.R. Menter, Two-equation eddy-viscosity turbulence models for engineering applications, AIAA J. 32 (1994) 1598–1605, http://dx.doi.org/10.2514/3.12149.

[43] A. Azad, A. Abid, C. Mithun, M. Hasan, R. Hossain, M. Rahman, Effect of Richardson number on transient double diffusive mixed convection: A thermo-hydrodynamic study, Int. J. Thermofluids 17 (2022) http://dx.doi.org/10.1016/j.ijft.2022.100273, 100273–100273.

[44] I. Ataei-Dadavi, M. Chakkingal, S. Kenjeres, C.R. Kleijn, M.J. Tummers, Experiments on mixed convection in a vented differentially side-heated cavity filled with a coarse porous medium, Int. J. Heat Mass Transfer 149 (2019) http://dx.doi.org/10.1016/j.ijheatmasstransfer.2019.119238, 119238–119238.

[45] J.J. Niemela, L. Skrbek, K.R. Sreenivasan, R.J. Donnelly, Turbulent convection at very high Rayleigh numbers, Nature 404 (2000) 837–840, http://dx.doi.org/10.1038/35009036.

[46] H.R. Nagendra, M.A. Tirunarayanan, A. Ramachandran, Laminar free convection from vertical cylinders with uniform heat flux, J. Heat Transf. 92 (1970) 191–194, http://dx.doi.org/10.1115/1.3449629.

[47] O. Ustun, M.L. Wong, D. Aslangil, Effects of Atwood number and isothermal stratification strength on single-mode compressible Rayleigh–Taylor instability, Phys. D Nonlinear Phenom. 476 (2025) http://dx.doi.org/10.1016/j.physd.2025.134644, 134644–134644.

[48] J.S. Turner, Buoyancy effects in fluids, Cambridge Monogr. Mech. (1973) http://dx.doi.org/10.1017/cbo9780511608827.

[49] M.J. de Lemos, M. Assato, Turbulence structure and heat transfer in a sudden expansion with a porous insert using linear and non-linear turbulence models, Int. J. Therm. Sci. 141 (2019) 1–13, http://dx.doi.org/10.1016/j.ijthermalsci.2019.03.025.

[50] M. Barnes, G.A. Rosi, D.E. Rival, Attenuation of shear-layer instabilities in steady and pulsatile axisymmetric shear-thinning flows, J. Fluid Mech. 1003 (2025) http://dx.doi.org/10.1017/jfm.2024.1144.